

## Article

# Development of High-Energy $\mu$ -X-ray Fluorescence and X-ray Absorption Fine Structure for the Distribution and Speciation of Rare Earth Elements in Natural Samples

Makoto Nagasawa<sup>1</sup>, Oki Sekizawa<sup>2</sup>, Kiyofumi Nitta<sup>2</sup>, Teruhiko Kashiwabara<sup>3</sup> and Yoshio Takahashi<sup>1,4,\*</sup> 

<sup>1</sup> Department of Earth and Planetary Science, Graduate School of Science, The University of Tokyo, Tokyo 113-0033, Japan; m.nagasawa71358@eps.s.u-tokyo.ac.jp

<sup>2</sup> Japan Synchrotron Radiation Research Institute (JASRI), Hyogo 679-5198, Japan; sekizawa@spring8.or.jp (O.S.); nittak@spring8.or.jp (K.N.)

<sup>3</sup> Submarine Resources Research Center (SRRC), Japan Agency for Marine-Earth Science and Technology (JAMSTEC), Yokosuka 237-0061, Japan; teruhiko-kashiwa@jamstec.go.jp

<sup>4</sup> Photon Factory, Institute of Materials Structure Science, High Energy Accelerator Research Organization (KEK), Tsukuba, Ibaraki 305-0801, Japan

\* Correspondence: ytakaha@eps.s.u-tokyo.ac.jp; Tel.: +81-3-5841-4517

**Abstract:** Micro-X-ray fluorescence and X-ray absorption fine structure ( $\mu$ -XRF-XAFS) is one of the most powerful tools to identify the distribution and speciation of trace elements in natural samples with  $\mu\text{m}$  spatial resolution. However, conventional  $\mu$ -XRF-XAFS studies applied to rare earth elements (REEs: lanthanide elements + Y in this study) are mainly limited to their L-edges and L lines (except for Y) that are subject to strong interferences from other elements (mainly transition metals). In this study, we extend  $\mu$ -XRF-XAFS to the higher energy region (HE- $\mu$ -XRF-XAFS) by using an incident X-ray microbeam (size: ca.  $1 \times 1 \mu\text{m}^2$ ) between 38 and 54 keV to realize K-edge excitation lanthanide analysis without interferences from other elements at the BL37XU beamline, SPring-8 (Japan). This method enables us to simultaneously analyze (i) REE patterns (from La to Dy), (ii) XAFS spectra, and (iii)  $\mu\text{m}$ -scale distribution of each REE in the natural sample. The proposed method also realizes the simultaneous application of  $\mu$ -XAFS at low (e.g., Fe K-edge) and high (lanthanide K-edges) energy at the same spot without changing the setup of the  $\mu$ -XRF-XAFS system using the detuning technique.

**Keywords:** high energy  $\mu$ -XRF-XAFS; rare earth elements (REEs); K-edges and K lines of REEs; speciation; REE pattern; weathered granite



**Citation:** Nagasawa, M.; Sekizawa, O.; Nitta, K.; Kashiwabara, T.; Takahashi, Y. Development of High-Energy  $\mu$ -X-ray Fluorescence and X-ray Absorption Fine Structure for the Distribution and Speciation of Rare Earth Elements in Natural Samples. *Minerals* **2023**, *13*, 746. <https://doi.org/10.3390/min13060746>

Academic Editor: Olivier Proux

Received: 6 April 2023

Revised: 23 May 2023

Accepted: 24 May 2023

Published: 30 May 2023



**Copyright:** © 2023 by the authors. Licensee MDPI, Basel, Switzerland. This article is an open access article distributed under the terms and conditions of the Creative Commons Attribution (CC BY) license (<https://creativecommons.org/licenses/by/4.0/>).

## 1. Introduction

Rare earth elements (REEs), which refer to elements including Y and lanthanide group elements from La to Lu but not Sc in this study, are important as geochemical tracers in earth and planetary sciences. The reason is that the relative abundances of REEs in natural systems reflect the distribution of elements controlled by ionic size based on their coherent chemical properties [1,2]. In the 21st century, REEs are also known as essential elements in high technology and green technology industries, and thereby attract research on their enrichment in natural samples in various systems. For example, REEs on land surfaces and the seafloor such as (i) ion-adsorption type deposits (IAD)—which mainly consist of weathered granite accumulating REE ions by adsorption reaction—and (ii) REE mud and ferromanganese crusts/nodules, respectively, have been examined [3–8]. These previous studies state that the speciation of REEs in natural samples is essential to understand their enrichment process, and thus the development of analytical methods for REEs is important not only for their abundance but also for their chemical states. Among various speciation methods, X-ray absorption fine structure (XAFS) spectroscopy has been applied to REEs including the following: (i) X-ray absorption near-edge structure (XANES) for determining

valences of Ce and Eu in natural samples [9–13] and (ii) local structure around the REE atom at the molecular scale by extended X-ray absorption fine structure (EXAFS) for microbial and deep sea REE mud [5,14]

Furthermore, the application of microanalyses in the local region (e.g., <30  $\mu\text{m}$ ) both for REE abundances and speciation can be a powerful tool to better understand their migration in natural systems. For this purpose, X-ray microbeam analysis is an important candidate, given that  $\mu\text{-XRF}$  mapping and  $\mu\text{-XAFS}$  analysis within a region of interest using X-ray microbeams obtained from synchrotron radiation sources ( $\mu\text{-XRF-XAFS}$ ) fulfill both requirements for the analysis of REEs in natural samples. Compared to methods using laser ablation, electron beam, or ion beam, the  $\mu\text{-XRF-XAFS}$  can reveal the micro-scale distribution (by  $\mu\text{-XRF}$ ) and the atomic-level information (by  $\mu\text{-XAFS}$ ) of REEs with minimal damage to the sample [3,15,16].

These X-ray microbeam analyses for REEs are often performed using their L-edges and L lines (except for Y) because K-edge excitation of REEs requires high energy X-rays (>38.9 keV for La K-edge). Thus, realizing a stabilized high-energy X-ray microbeam with sufficient photon flux is difficult. By comparison, the use of L lines of REEs to measure L-edge XAFS for REEs is subject to interferences from emission lines of other elements such as transition metals. Especially for natural samples, various metal ions such as Fe, Mn, Ti, or Ba can cause interferences in XRF and fluorescence XAFS analyses.

Recently, a newly developed system of Kirkpatrick–Baez (KB) mirror [17] installed in BL37XU, SPring-8 (Hyogo, Japan) [18] has allowed for the possibility to realize high-energy X-ray microbeams up to 55 keV. This study, therefore, took advantage of the fact that REE K lines are not affected by fluorescent X-rays of other elements when we use the K-edge at high energy regions (>38.9 keV), and developed a practical application using the new KB mirror system as the High-Energy  $\mu\text{-XRF-XAFS}$  (HE- $\mu\text{-XRF-XAFS}$ ). The applicable energy range is practically limited to K-edges from La to Dy due to the reflection efficiency of the KB mirror as discussed below. However, the energy range covers most of the REEs that can generally be measured by XRF above the detection limit (mg/kg order).

There are several beamlines where X-ray absorption spectra using a microbeam in the high-energy region can be measured. For example, the ID24-DCM beamline [19] at European Synchrotron Radiation Facility (ESRF; Grenoble, France) has a wide energy range (5–45 keV) available for  $\mu\text{-XRF}$ . It is also possible to conduct  $\mu\text{-XRF}$  and XRF-CT up to 90 keV at beamline ID15a in ESRF [20]. However,  $\mu\text{-XAFS}$  over 40 keV has not been examined. In this study, we measured the Nd K-edge (43.6 keV) XAFS using X-ray microbeams. Although XAFS at high energy such as Dy K-edge has been reported [21] for bulk XAFS analysis, X-ray microbeam measurement for XAFS above 43 keV is very limited, suggesting the novelty of this study.

In using a wide energy range to cover K-edges XAFS of major elements (e.g., Fe, Mn, and Ti) and REEs, we generally need to change the optical system to measure XAFS spectra for the low and high energy regions (LER and HER, respectively). For example, Fe (a major element in various minerals) K-edge is at 7.1 keV, while that of La is 38.9 keV. In such an experiment, different optical setups of the incident X-ray are used in general for (i) LER (e.g., 7–20 keV) and (ii) HER (>20 keV). The main reasons are as follows: (i) the limitation of the energy range covered by a double-crystal monochromator (DCM) and (ii) the use of total reflection mirrors to suppress high-order harmonics in the synchrotron radiation X-ray, which is essential for acquiring of high-quality XAFS spectra. However, the use of the two optical setups with different DCMs and angles of the total reflection mirrors may shift the position of the X-ray microbeam/submicron beam, which causes difficulties to analyze the same exact spot between the two setups (e.g., the spots analyzed at LER mode for major elements and at HER mode for REEs). In addition, switching to the other setup, which takes more than 5–10 h, and independent mapping analysis to find the hot spot, which takes at least several hours, lead to a time-consuming analysis. Such a long measurement time results in high damage to the sample due to prolonged exposure to X-rays and can be a problem, especially for the chemical state analysis of various elements.

In this study, we have made it possible to perform the HE- $\mu$ -XRF-XAFS experiment over a wide energy range using a single optical setup. Thus, we can simultaneously analyze the chemical species of the major elements in the host phase and those of REEs in the local region at micron/submicron scales.

## 2. Materials and Methods

### 2.1. Samples

The NIST standard reference material (SRM) 610, which is trace-element-doped SiO<sub>2</sub> glass, was used as the primary standard material to determine the REE concentrations in natural samples [22]. The sample is spatially homogeneous and has been used for various local analyses including secondary ion mass spectrometry (SIMS) and laser ablation inductively coupled plasma mass spectrometry (LA-ICP-MS) [23–26]. A natural reference sample used in this study is JMn-1, a standard reference material issued by the Geological Survey of Japan (Tsukuba City, Ibaraki) for marine ferromanganese oxides collected from the Pacific seafloor [27]. Marine ferromanganese oxides are considered to be an important resource of various metallic elements [3,28]. The JMn-1 was supplied as a powdered sample, where the minerals are generally nanoparticles, smaller than the size of the beam used (ca.  $1 \times 1 \mu\text{m}^2$ ). Thus, the sample is spatially homogeneous for the  $\mu$ -XRF analysis. The powdered samples of NIST SRM 610 and JMn-1 were shaped into a pellet (diameter: 1 cm; thickness: 50  $\mu\text{m}$ ) using a press without a binder for the HE- $\mu$ -XRF analysis. Certified values of bulk major elements (as oxides) and REE concentrations in NIST SRM 610 and JMn-1 were reported by Pearce et al. [22] and Terashima et al. [27], respectively (Table 1).

**Table 1.** Major element (oxides) and REE concentrations of the SWG sample, NIST SRM 610 [22], and JMn-1 [27]. Ba concentration was also listed as a potential interference element for REEs in XRF and XAFS analysis. Abbreviation: SWG = strongly weathered granite.

Element	SWG Sample	NIST SRM 610	JMn-1
SiO <sub>2</sub>	69.7 (wt.%)	72 (wt.%)	14.11 (wt.%)
Al <sub>2</sub> O <sub>3</sub>	16.2	2.0	4.30
Fe <sub>2</sub> O <sub>3</sub>	1.34	0.0654	14.4
MnO	0.03	0.0560	33.09
MgO	0.36	0.0772	3.12
CaO	N.D.	0.12	2.91
Na <sub>2</sub> O	0.19	0.12	2.80
K <sub>2</sub> O	3.87	0.0691	0.94
TiO <sub>2</sub>	0.03	0.0724	1.06
P <sub>2</sub> O <sub>5</sub>	N.D.	0.0785	0.54
Y	2040 (mg/kg)	450 (mg/kg)	111 (mg/kg)
Ba	49.7	424	1714
La	189	457	122
Ce	21.2	448	277
Pr	65.0	430	31.4
Nd	280	431	137
Sm	123	451	30.2
Eu	0.660	461	7.6
Gd	227	420	29.8
Tb	46.6	443	4.8
Dy	340	427	28.3
Ho	66.8	449	5.8
Er	169	426	14.6
Tm	22.3	420	2.1
Yb	139	462	13.8
Lu	19.4	435	2.1

Another natural sample used in this study is a strongly weathered granite (SWG) sample collected in Otsu City, Shiga, Japan, details of which will be reported elsewhere [29]. Based on the powder X-ray diffraction (XRD) pattern (Figure 1), this sample is a typical weathered granite consisting of quartz, alkali feldspar, mica, and their weathering products such as smectite and kaolin group minerals. The XRD measurement was carried out on the powdered sample using an X-ray diffractometer (RINT-2000, Rigaku, Tokyo, Japan). Bulk chemical compositions of major elements (as oxides) and REEs were determined (Table 1) by (i) XRF analysis of the fused-bead sample using an XRF spectrometer (Axios, PANalytical, Tokyo, Japan) and (ii) inductively coupled plasma mass spectrometry (ICP-MS; 7700cs, Agilent, Tokyo, Japan) for the solution containing REEs obtained by the decomposition of the SWG sample using mixed acids, respectively [30]. For the HE- $\mu$ -XRF-XAFS analyses, the SWG sample was formed into a double-sided polished thin section of 50  $\mu$ m thickness using Epo Fix Resin (Struers, Tokyo, Japan).

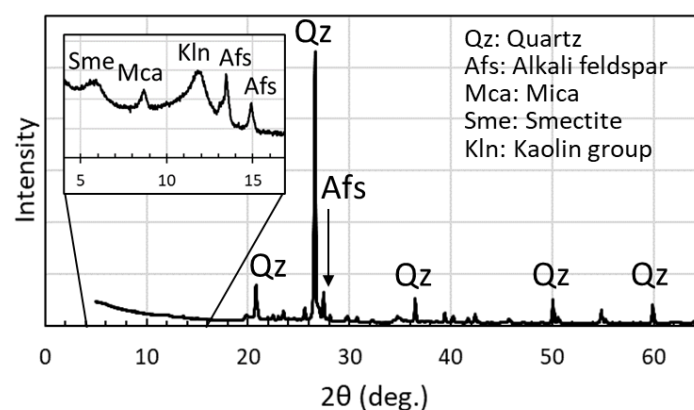


**Figure 1.** Powder XRD pattern of the SWG sample.

## 2.2. Micro-XRF Analysis

In this study, the incident X-ray energy was typically 54 keV for REE analysis and the beam size was smaller than 1  $\mu$ m (horizontal)  $\times$  1  $\mu$ m (vertical) focused by the KB mirror system at BL37XU in SPring-8 [18]. The elliptical-shaped KB mirror, made of silicon, was coated with Pt (100 nm) and Rh (100 nm), and the Pt side was used. The glancing angle was 1.6 and 1.5 mrad for horizontal and vertical focusing mirrors, respectively. The mirror size was 200  $\times$  50  $\times$  50 mm<sup>3</sup> and 150  $\times$  50  $\times$  50 mm<sup>3</sup> with surface roughness (root mean square: RMS) <0.35 nm and <0.50 nm for the horizontal and vertical mirrors, respectively. The focal length was 360 mm and 175 mm for the horizontal and vertical mirrors, respectively.

The step size and one-line scan time of the XRF mapping were typically 1–5  $\mu$ m and 20 s, respectively. A germanium (Ge) single-element semiconductor detector (EGX10-06-CP5-PLUS-WC; Mirion Technologies Inc., Atlanta, GA, USA) was used as the XRF detector.

To quantify the REE concentration, the NIST SRM 610 was measured under the same condition as that of the natural samples. The REE concentrations ( $=[REE]$ ) in the local area were calculated by using Equation (1) and each REE pattern was obtained without the absorption effect correction due to high energy. This is because more than 99% and 96% of the hard X-rays (>33 keV) can be transmitted by a 50  $\mu$ m thin section of (i) NIST SRM 610 and SWG and (ii) JMn-1 with their chemical compositions (Table 1), respectively, based on the calculation using the "X-ray Interaction With Matter" software on the website of Advanced Light Source (Berkeley, CA, USA) [31]. The results confirmed that the absorption of X-rays by the matrix materials can be negligible in HER. As a result,  $[REE]$  in the sample ( $=[REE]_{sample}$ ) can be determined as

$$[REE]_{sample} = [REE]_{NIST} \times \frac{A - XRF_{sample} / (T_{sample} \cdot I_{0sample})}{A - XRF_{NIST} / (T_{NIST} \cdot I_{0NIST})} \quad (1)$$

where  $A$ -XRF,  $T$ , and  $I_0$  indicate areas of REE  $K\alpha$  line peak, sample thickness, and intensity of the incident X-ray, respectively. The area of each peak was determined by using PyMCA software (ESRF, Grenoble, France) [32] after subtraction of background and possible interferences from XRF of other elements. REE abundances in CI chondrite (Orgueil) were used for the normalization of REE to obtain REE patterns [33].

### 2.3. Micro-XAFS Analysis

EXAFS analysis for La and Nd K-edges and XANES analysis for Fe K-edge were carried out to reveal the adsorption structure of REEs and mineralogy of the host phase. The energy was calibrated by the maximum of the white line of the standard material ( $\text{La}_2\text{O}_3$ ) assigned to 38.934 keV. The XAFS spectra of the standard samples were obtained in transmission mode, whereas those of the natural samples were in fluorescence mode. The EXAFS spectra were analyzed following a standard fitting procedure [34] using REX2000 software (Rigaku Co., Tokyo, Japan) and FEFF 7.02 (University of Washington, Seattle, WA, USA) [35]. Errors in the fitted parameters such as interatomic distance ( $R$ ), coordination number (CN), and Debye–Waller factor ( $\sigma$ ) were estimated to be generally  $\pm 0.02 \text{ \AA}$ ,  $\pm 20\%$ , and  $\pm 20\%$ , respectively [36]. Given that CN and  $\sigma$  are correlated parameters with relatively large errors, CN was fixed in this study.

## 3. Results and Discussion

### 3.1. Optical Setup to Cover Wide Energy Range

The primary aim of this study is to extend the  $\mu$ -XRF-XAFS analysis to K-edges of REEs (up to Dy) to avoid possible interferences that occur when using L-edges and L lines without state-of-the-art high-energy resolution detectors such as the crystal analyzer system [19] or transition-edge sensor (TES) detector [37]. For this purpose, the KB mirror applicable to HER was used to obtain submicron X-rays. In such cases, a different optical setup is generally used to cover a wide energy range (e.g., 7–55 keV) for examining elements from major to trace elements by  $\mu$ -XRF-XAFS analysis [38]. For example, two DCMs, Si(111) and Si(511) are available at beamline BL37XU in SPring-8, but their applicable energy ranges are limited to 4.9–37.7 keV and 13–113 keV, respectively. In addition, the removal of high-order harmonics is essential to use low-energy X-rays (e.g., 7.1 keV for Fe K-edge XAFS) for high-quality XAFS measurement, but the use of total reflection mirrors prevents that of high-energy incident X-ray under the same optical setup. If we can examine the entire energy region using a single optical setup, then we can achieve a more effective and efficient speciation analysis of REEs and major elements in a much shorter time.

To solve these problems, we removed the high-order harmonics by detuning the second crystal of the DCM [39,40] for the LER measurement (7–15 keV), while we used third-order X-ray using Si(111) as DCM to examine HER (30–55 keV). In the latter setup, first-order light can be eliminated by inserting an absorber (e.g., Cu foil) before the  $I_0$  detector (ion chamber to determine the intensity of incident X-ray) as shown in Figure 2, when we need to reduce the total signals entering the Ge detector. When XRF mapping of various elements is obtained, however, the first-order light can be useful to excite lighter elements because the excitation efficiency of the lighter elements by HER X-rays is not high. When we measured EXAFS at high energy such as at La and Nd K-edges by the third-order X-ray, the first-order light was completely eliminated by 0.2 mm of Cu foil.

By adjusting the KB mirror, we obtained the minimum size of the X-ray microbeam of 152 nm (horizontal) and 80 nm (vertical) with a photon flux of  $1.2 \times 10^8 \cdot \text{s}^{-1}$  at 40 keV (Figure 3a). When the concentration of some REEs in our sample is low, a larger beam may be more effective (Figure 3b). For this purpose, the submicron beam such as ca. 800–1000 nm (h) and 800–1000 nm (v) was mainly used in this study with a more intense beam, ca.  $5 \times 10^9 \cdot \text{s}^{-1}$ .

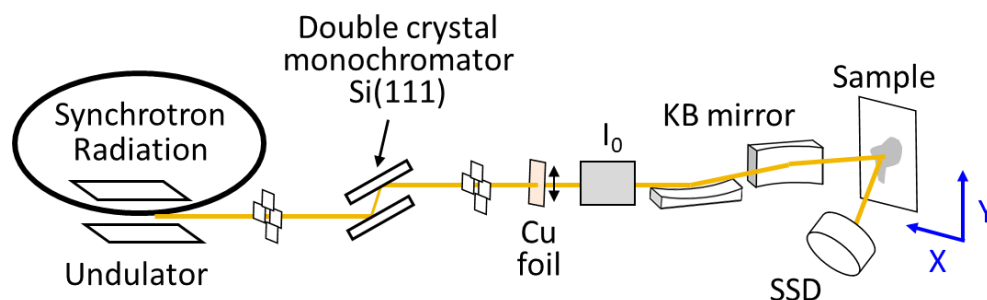


**Figure 2.** Schematic of optical and measurement system of HE- $\mu$ -XRF-XAFS at beamline BL37XU in SPring-8.

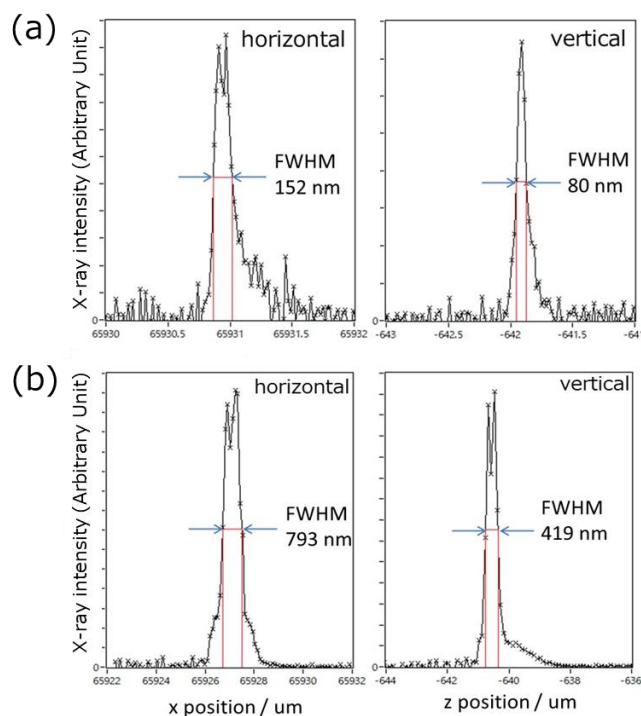


**Figure 3.** Beam size measured by knife-edge method; (a) Minimum beam with the photon flux of  $1.2 \times 10^8 \cdot \text{s}^{-1}$  at 40 keV, (b) An example of a larger beam with more photon flux. Abbreviation: FWHM = full width at half maximum.

The selection of the incident energy is critical for the HE-XRF analysis for REE studies. The flux of the beam decreases as the energy increase, because (i) the original photon flux before the KB mirror decreases from  $5.2 \times 10^9 \cdot \text{s}^{-1}$  at 45 keV to  $3.0 \times 10^8 \cdot \text{s}^{-1}$  at 55 keV using  $1 \times 1 \mu\text{m}^2$  beam (Figure 4a), and (ii) the reflectance of the KB mirror also decreases from 62% at 40 keV to 5.2% at 55 keV (Figure 4b).

On the other hand, absolute abundances of REEs generally decrease from light REEs (LREEs, e.g., La with  $Z$  (atomic number) = 57) to heavy REEs (HREEs, e.g., Lu with  $Z = 72$ ) with lower abundances for odd  $Z$  elements relative to the neighboring even  $Z$  elements. Given that our main aim is to apply the method to natural samples, the energy dependence of the photon flux at the sample position was compared with the abundances of REEs in CI chondrite (Figure 4c), which is considered Earth's parent materials [33]. This comparison shows that the low abundance of Ho and low intensity of the microbeam at the energy above its K-edge (55.618 keV) cause difficulties in measuring the Ho  $K\alpha$  line. Thus, we decided to use 54 keV X-ray as the incident X-ray for the  $\mu$ -XRF analysis of REEs with photon flux above  $10^7 \cdot \text{s}^{-1}$ . To increase the flux, we can use a lower glancing angle. When the incident angle of an X-ray mirror becomes shallower, however, the mirror aperture becomes smaller, which limits the available beam. To increase the sensitivity of the entire

system, using a multielement Ge detector instead of a single element used in this study will be effective.

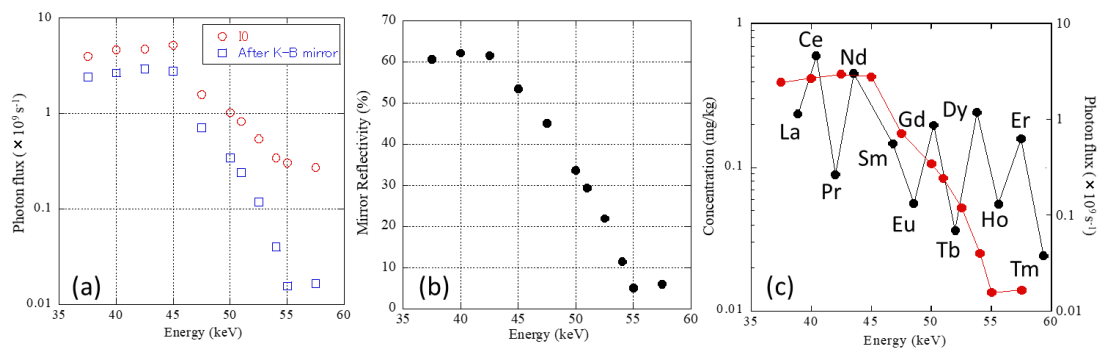


**Figure 4.** Energy dependence of (a) photon flux before and after KB mirror (counted by  $I_0$  and  $I_1$  detectors, respectively), (b) reflectance of KB mirror, and (c) photon flux after the KB mirror (in red) superimposed by the abundances of REEs in CI chondrite (in black).

When we use the two setups of (i) HER without detuning and (ii) LER with 60% detuning, one may be concerned whether the position of the beam can be shifted, given that the fine adjustment of the second crystal in the DCM can cause a shift of the incident X-ray. However, the shift of the beam determined by the knife-edge method [41] using a Ta blade was restricted within  $\pm 0.5 \mu\text{m}$  (precision of this method is approximately 4%; [42]) for both vertical and horizontal directions (Figure 5). This shift of less than  $0.5 \mu\text{m}$  is good enough considering that the beam size here is  $1 \mu\text{m}$ . This result showed that the detuning does not affect the beam position and is effective to attenuate high-order harmonics when we use the setup for LER.

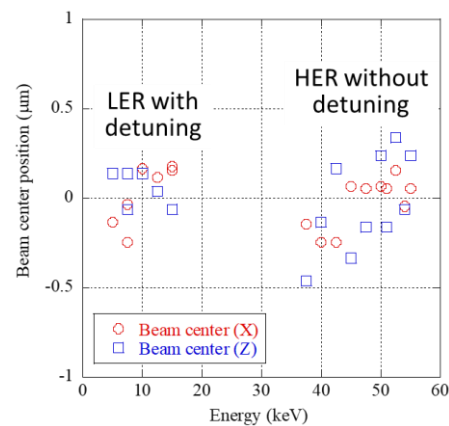


**Figure 5.** Energy dependence of beam center position.

### 3.2. HE-XRF Analysis

Figure 6 is the XRF spectra for NIST SRM 610 and JMn-1 samples. They clearly showed  $K\alpha_1$  and  $K\alpha_2$  peaks for each lanthanide element from La to Dy. The XRF intensity was determined by fitting each peak using PyMCA [32] while removing interferences of XRF from other elements. Deconvolution of each peak in the spectra for the correction of interfered peaks was highly needed for natural samples (an example is shown in Figure 7) such as interferences of (a)  $K\beta$  emission of Ba and lighter REEs on  $K\alpha_1$  of relatively heavier REEs and (b)  $K\alpha_2$  of elements with odd atomic numbers on  $K\alpha_1$  of adjacent elements with even atomic numbers. The examples of case (a) are (i) Ba  $K\beta_{1,3}$  (36.378 and 36.304 keV, respectively), on Pr  $K\alpha_1$  (36.026 keV) and (ii) Pr  $K\beta_2$  (41.754 keV) on Eu  $K\alpha_1$  (41.542 keV). By comparison, the degree of interferences of case (b) such as (i) Gd  $K\alpha_2$  on Eu  $K\alpha_1$  and (ii) Dy  $K\alpha_2$  on Tb  $K\alpha_1$  is not severe. After the corrections of the interferences, the intensity was normalized by that of the incident X-ray ( $I_0$ ) as shown in Equation (1).

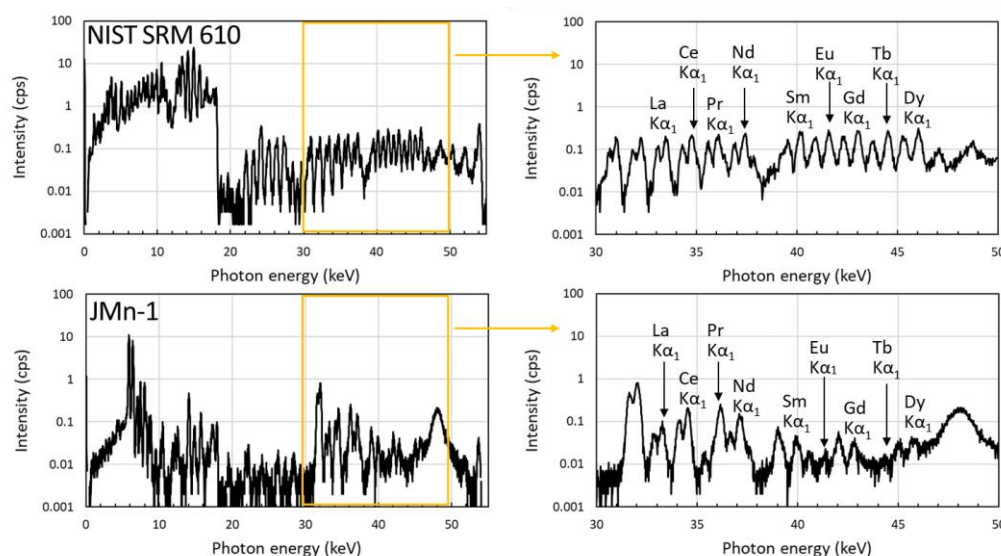


**Figure 6.** XRF spectra for NIST SRM 610 and JMn-1 samples irradiated at 54 keV. Yellow rectangle area (30–50 keV in the left figures) was expanded in the right figures.

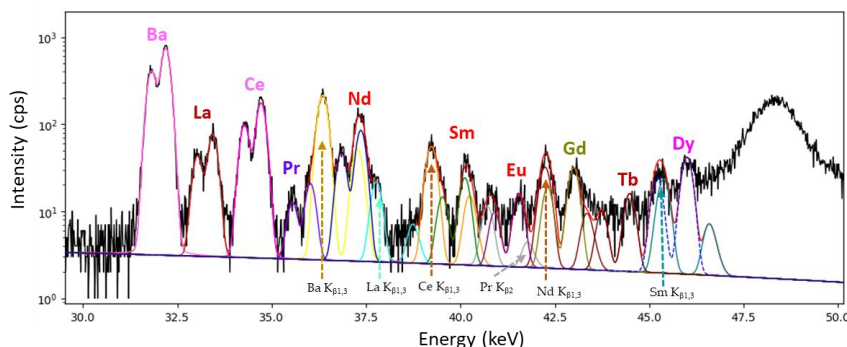


**Figure 7.** XRF spectra irradiated at 54 keV for JMn-1 with deconvoluted peaks by PyMCA.

The REE pattern normalized by CI-chondrite was obtained for the JMn-1 sample based on the determination of their REE concentrations by HE-XRF (Figure 8a, Table 2). As discussed above, the determination of concentrations of Eu and Tb was not possible due to their low abundances and interferences of XRF from other elements. The concentrations of the other seven elements (La, Ce, Pr, Nd, Sm, Gd, and Dy) were similar to the certified values in Terashima et al. [27] with a relative difference smaller than 17% for any examined REE except for Pr (27%) and Dy (33%). These results suggest that the direct determination of REE concentration by HE- $\mu$ -XRF can be used to obtain REE patterns with a spatial resolution of less than 1  $\mu$ m.

**Table 2.** Results of HE-XRF quantification.

Element	JMn-1 (ppm)	Point 1 (ppm)	Point 2 (ppm)
La	140 ± 3	119 ± 5	8797 ± 114
Ce	280 ± 4	7.60 ± 1.72	10433 ± 115
Pr	23.0 ± 1.5	27.7 ± 2.7	863 ± 31
Nd	114 ± 3	176.9 ± 5.5	2706 ± 54
Sm	29.3 ± 1.4	83.1 ± 3.7	329 ± 28
Eu	N.D.	N.D.	N.D.
Gd	34.9 ± 1.2	156 ± 5	173 ± 15
Tb	N.D.	30.9 ± 3.0	N.D.
Dy	37.6 ± 1.2	217 ± 6	121 ± 4

N.D.—Not Determined.

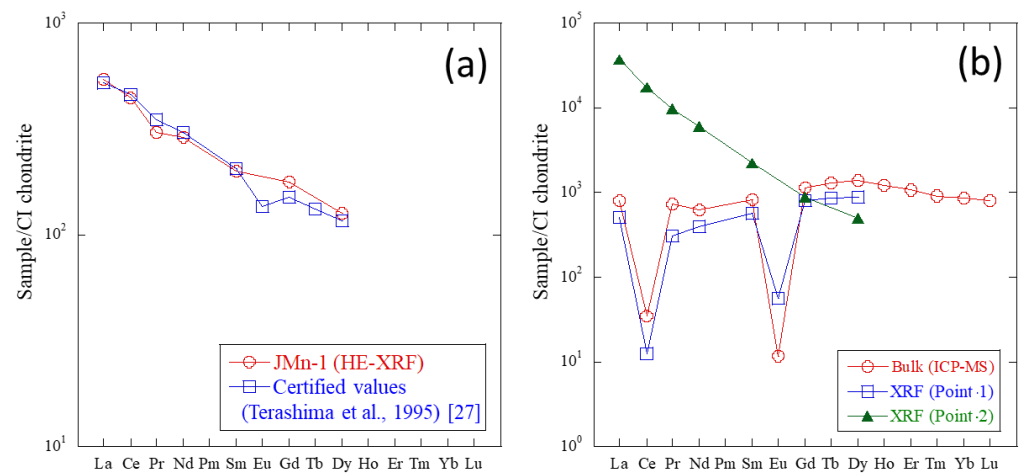


**Figure 8.** REE patterns normalized by CI-chondrite of (a) JMn-1 and (b) SWG samples based on the determination of their REE concentrations by HE-XRF.

3.3. Micro-XRF Analysis

Micro-XRF mapping using the ca.  $1 \times 1 \mu\text{m}^2$  beam was carried out on the double-sided polished SWG sample.  $K\alpha_1$  lines of Y, La, Ce, and Nd (Figure 9a) were used to illustrate the distributions of HREEs and LREEs. As a result, two types of REE enrichment were observed (Figure 9b). One is the widely distributed REE enrichment (Point 1) and the other is the REE hot spot (Point 2).

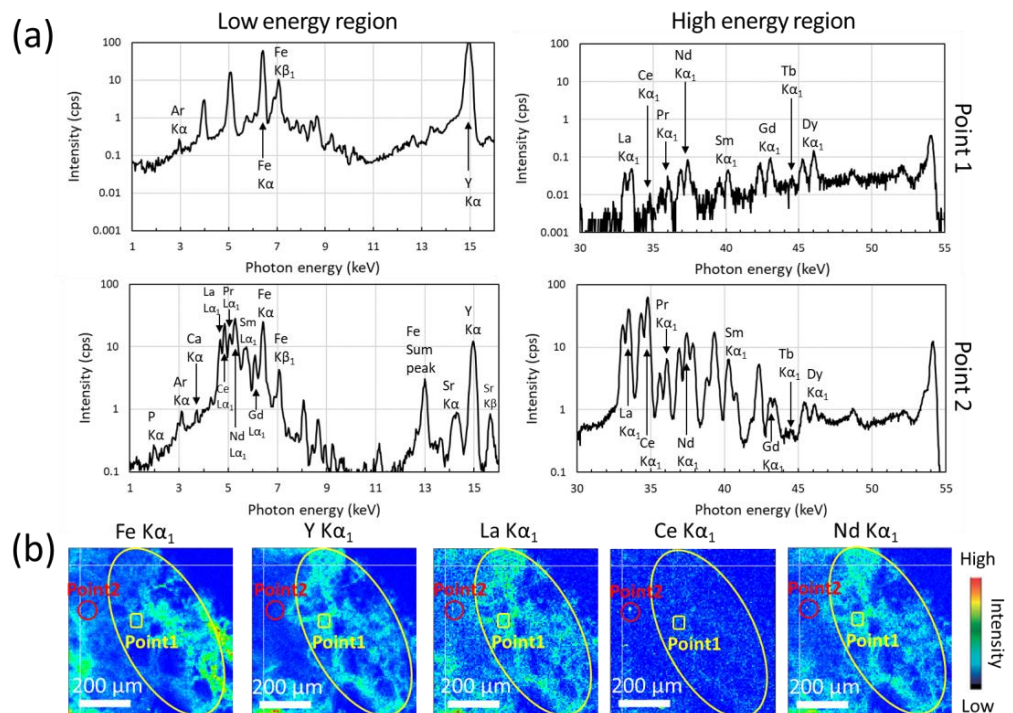


**Figure 9.** (a)  $\mu$ -XRF spectra of Points 1 and 2, (b) distribution of each element by  $\mu$ -XRF mapping.

The high concentration of REEs (Y, La, and Nd) at Point 1 was found in the grain boundaries among primary minerals (e.g., quartz, feldspar, and micas according to the XRD pattern in Figure 1). In addition, the distribution of REEs is relatively well correlated with that of Fe, suggesting that REEs are concentrated in Fe-bearing minerals. These results suggest that REEs are adsorbed on clay minerals at Point 1. In fact, the XRD of the bulk sample (Figure 1) shows the peaks of smectite and kaolin group minerals at  $2\theta =$  approximately  $5.7^\circ$  and  $12^\circ$ , respectively. Owing to the large cation exchange capacity

(CEC), these clay minerals can be the host phases of  $\text{REE}^{3+}$  adsorbed from pore water. By contrast, Ce was not concentrated in the same area. This may be because only Ce is immobile due to the oxidation to  $\text{Ce}^{4+}$  during the weathering process in which other REEs can be dissolved in pore water and finally adsorbed in the grain boundary [7]. The XRF maps of REEs in the grain boundary were obtained because K lines of REEs were clearly detected without interferences at the micron/submicron scale by the excitation of K-edge using HE incident X-ray. As shown in Figure 9a, the L lines of REEs located below 10 keV cannot be detected at Point 1 due to interferences of other elements.

The REE pattern of Point 1 obtained by the  $\mu$ -XRF data exhibits a large negative Ce anomaly (Figure 8b). Bulk REE concentrations measured by ICP-MS were also plotted for comparison to Point 1. They showed similar REE patterns with negative Ce anomaly, showing that (i) the bulk REE pattern is represented by that of Point 1 and (ii) most of the REEs in the SWG sample are secondarily adsorbed within the sample. This is a typical characteristic of REEs in SWG, or IAD, as reported in many studies [43–45].

REEs (La, Ce, and Nd) were also concentrated at Point 2 (size < 10  $\mu\text{m}$ ) but in a different manner from that of Point 1: (i) Fe was not found at the spot and (ii) REEs including Ce but not Y were concentrated. This may be because Point 2 is the igneous/hydrothermal REE-bearing accessory mineral such as apatite and/or zircon without Ce fractionation from other REEs. Here, the  $\mu$ -XRF spectrum at Point 2 (Figure 9a) indicates the presence of Ca (3.7 keV), P (2.0 keV), and Sr (14.2 and 15.8 keV for  $\text{K}\alpha$  and  $\text{K}\beta$ , respectively). The REE pattern of Point 2 indicates an LREE-rich pattern with a much higher concentration than the bulk. These findings suggest that Point 2 is an apatite particle [46]. Further identification of the mineral by scanning electron microscopy (SEM) was difficult since the mineral is not present at the surface of the thin section but buried within the sample, which can be still detected by XRF with much deeper probing depths especially using HE X-rays.

### 3.4. Micro-XAFS

Micro-XAFS was also measured at Points 1 and 2 (Figure 10). Particularly, we successfully obtain EXAFS spectra for Point 2. Given that XANES in HER is featureless due to lifetime broadening compared with that in LER [47], the measurement of EXAFS is more important than XANES in HER. In this study, La K-edge EXAFS spectra were mainly collected. Figure 10a shows the k-space EXAFS spectra of the sample (bulk and Point 2) and reference materials including hydrated  $\text{La}^{3+}$  ion (= 0.05 M  $\text{La}(\text{NO}_3)_3$  solution),  $\text{La}^{3+}$  adsorbed on apatite and montmorillonite,  $\text{LaPO}_4$ , and monazite. R-space EXAFS spectra of the sample (bulk and Point 2) are also shown in Figure 10b. The results of the EXAFS curve fitting are shown in Table 3.

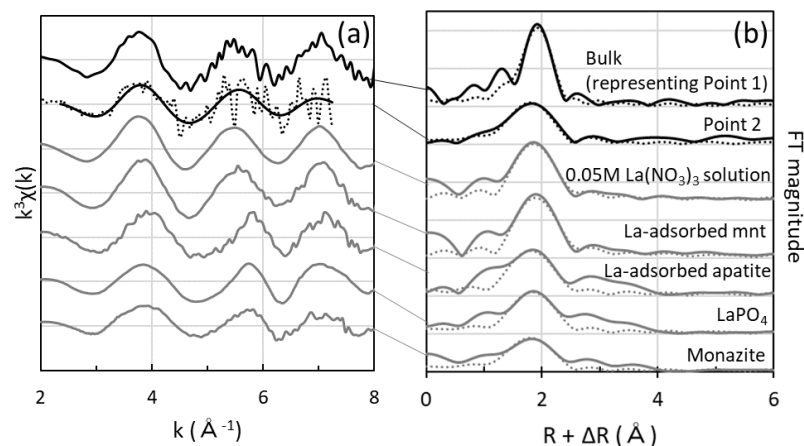


**Figure 10.** (a) La K-edge EXAFS spectra of the SWG sample (bulk and Point 2) and reference materials in k-space; Only for Point 2, original (k-space) and q-space spectrum is dotted and solid line, respectively. (b) La K-edge EXAFS spectra of the SWG sample (bulk and Point 2) and reference materials in R-space; dotted line is a fitting curve. Abbreviation: mnt = montmorillonite.

It was difficult to obtain a good quality spectrum for Point 1, but the fact that its REE pattern represents that of the bulk (Figure 8b) suggests a possible similarity with the bulk EXAFS spectrum. As shown in Figure 10, k-space spectra of the bulk sample, hydrated  $\text{La}^{3+}$ , and La-adsorbed montmorillonite are all similar. These spectra exhibit a single sinusoidal component, suggesting that there is little contribution of backscattered photoelectrons from any second neighboring atoms. This finding means that  $\text{La}^{3+}$  is present as a hydrated ion as an outer-sphere complex adsorbed on clay minerals in such areas. The La-O interatomic distance for the bulk sample, hydrated  $\text{La}^{3+}$ , and La-adsorbed montmorillonite were  $2.559 \pm 0.017$ ,  $2.560 \pm 0.025$ , and  $2.561 \pm 0.025$  Å, respectively (Table 3). This result is also consistent with that previously reported for hydrated  $\text{La}^{3+}$  (= 2.551 Å) [48]. The measurement of Fe K-edge XANES at Point 1 was also possible thanks to the applicable wide energy range established in this study to measure XANES for various elements/edges (Figure 11). The spectrum was successfully fitted mainly by a mixture of Fe in montmorillonite (53.2%) and illite (34.6%) (residual: 0.019%), which were also detected in the XRD pattern (Figure 1). These results suggest that the clay minerals are the host phase of La, or REEs other than Ce. The formation of an outer-sphere complex of REEs in clay minerals is the most important characteristic in SWG, or IAD [6,7,45].

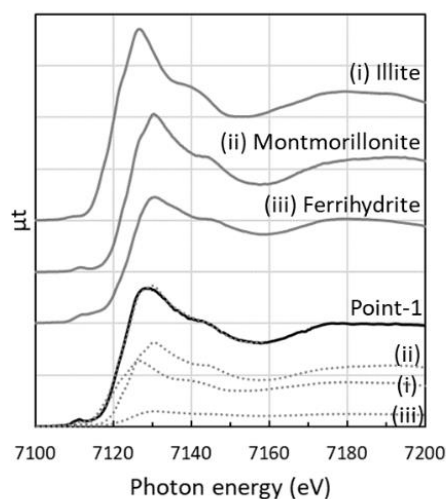


**Figure 11.** Fe K-edge XANES for Fe in the bulk sample. Solid line: spectra of Point 1 and reference materials (i)–(iii); dotted line: fitting line and contribution of each component from (i) to (iii).

Meanwhile, the k-space spectrum of Point 2, La-adsorbed apatite,  $\text{LaPO}_4$ , and monazite are similar to each other but somewhat different from that of hydrated  $\text{La}^{3+}$  in that (i) the height of a peak around  $k = 4 \text{ \AA}^{-1}$  for Point 2 is lower than that of hydrated  $\text{La}^{3+}$  and (ii) the k value of the next peak of Point 2 around  $k = 5.5\text{--}6 \text{ \AA}^{-1}$  is larger than that of hydrated  $\text{La}^{3+}$ . The La-O distance for La at Point 2 was  $2.515 \pm 0.026$  Å, slightly shorter than that for hydrated ion, but closer to La-O in La phosphate ( $2.495 \pm 0.022$ ,  $2.523 \pm 0.024$ ,  $2.511 \pm 0.016$  Å for La-adsorbed apatite,  $\text{LaPO}_4$ , and monazite, respectively, in Table 3). These values are also consistent with that previously reported for  $\text{LaPO}_4$  (=  $2.53 \pm 0.004$  Å) [49]. These features as well as the presence of P in the XRF spectrum (Figure 9a) suggest that the  $\text{La}^{3+}$  species is not a hydrated ion, but likely phosphate at Point 2.

At Point 2, Nd K-edge EXAFS was also obtained (Figure 12). The fitting results in the R-space (Table 3) show that the Nd-O distance is  $2.348 \pm 0.028$  Å, which is reasonable based on a previously reported value for Nd in phosphate glass ( $2.367 \pm 0.009$  Å; [50]). Considering the Nd-O distance of the hydrated  $\text{Nd}^{3+}$  ion ( $2.489$  Å; [49]), it is reasonable that REE-O distance of REE phosphate is shorter than that of hydrated  $\text{REE}^{3+}$  for both  $\text{La}^{3+}$  and  $\text{Nd}^{3+}$ . This fact is consistent with the speculation shown above that REE-phosphate is formed at Point 2.

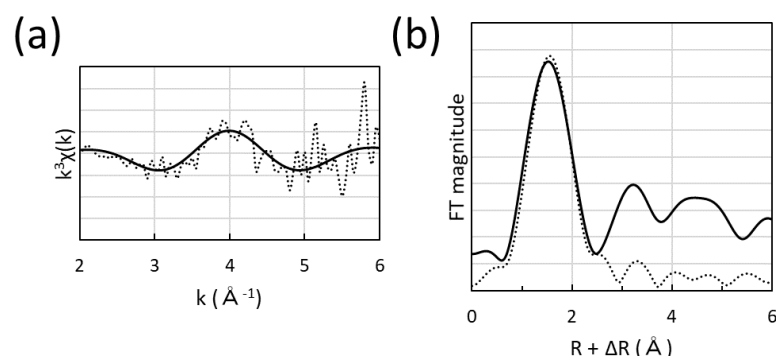


**Figure 12.** (a) Nd K-edge EXAFS spectra of the SWG sample (Point 2); original (k-space) and q-space spectrum is dotted and solid line, respectively. (b) Nd K-edge EXAFS spectra of the SWG sample (Point 2) in R-space; dotted line is a fitting curve.

Given that REEs in the phosphate are generally non-leachable [7,51], identification of leachable and non-leachable REEs in clay minerals and phosphate, respectively, by HE- $\mu$ -XRF-XAFS is important to characterize REEs in SWG. This means that the leaching behavior of REEs from SWG is closely related to REE species. Thus, HE- $\mu$ -XRF-XAFS analysis contributes to unraveling these chemical processes and the availability of REEs from resources. Although the host mineral of REEs in SWG cannot always be determined solely by HE- $\mu$ -XRF-XAFS, a combination of HE- $\mu$ -XRF-XAFS, SIMS, and transmission electron microscopy (TEM) can play an important role in understanding the chemical bonding of REEs, their abundances, and host minerals in SWG or other REE-bearing samples [45,52].

**Table 3.** Results of the EXAFS curve fitting for bulk (representing Point 1) and Point 2.

Sample	k Range ( $\text{\AA}^{-1}$ )	FT Range ( $\text{\AA}$ )	Shell	CN	R ( $\text{\AA}$ )	$\Delta E_0$ (eV)	$\sigma^2$ ( $\times 10^{-3} \text{\AA}^2$ )	Residual (%)
Bulk (Point 1)	2.35–7.25	1.19–2.57	La-O	9 *	$2.559 \pm 0.017$	$-3.40 \pm 1.70$	$9.8 \pm 2.6$	2.1
Point 2	2.35–7.25	0.89–2.55	La-O	9 *	$2.515 \pm 0.026$	$-5.39 \pm 2.51$	$16.4 \pm 4.1$	1.3
	1.65–6.05	0.58–2.52	Nd-O	9 *	$2.348 \pm 0.028$	$-12.3 \pm 2.22$	$18.8 \pm 5.5$	1.8
0.05 M $\text{La}(\text{NO}_3)_3$ solution	2.35–7.25	1.26–2.58	La-O	9 *	$2.560 \pm 0.025$	$-3.73 \pm 2.57$	$9.8 \pm 4.0$	0.91
La-adsorbed mnt	2.35–7.25	1.32–2.58	La-O	9 *	$2.561 \pm 0.025$	$-1.54 \pm 2.56$	$8.5 \pm 3.9$	0.95
La-adsorbed apatite	2.35–7.25	1.41–2.39	La-O	9 *	$2.495 \pm 0.022$	$-2.43 \pm 2.11$	$14.2 \pm 3.6$	0.057
$\text{LaPO}_4$	2.35–7.25	1.29–2.42	La-O	9 *	$2.523 \pm 0.024$	$-2.03 \pm 2.22$	$15.4 \pm 3.7$	0.59
Monazite	2.35–7.25	1.27–2.49	La-O	9 *	$2.511 \pm 0.016$	$-2.88 \pm 1.40$	$20.2 \pm 2.6$	1.1

\* The value was fixed at 9 during the fitting [53–55]. CN: coordination number; R: interatomic distance;  $\Delta E_0$  shift of threshold energy;  $\sigma$ : Debye-Waller factor. Abbreviation: mnt = montmorillonite.

#### 4. Conclusions

In this study, HE- $\mu$ -XRF-XAFS analysis was established for K-edge XAFS and XRF including K lines of REEs in natural samples by using an incident X-ray microbeam (size: ca.  $1 \times 1 \mu\text{m}^2$ ) between 38 and 54 keV. We removed high-order harmonics by detuning the second crystal of the DCM for low-energy regions (7–15 keV) while using a third-order X-ray with Si (111) as DCM for high-energy regions (38–55 keV). The results revealed that the detuning does not change the position of the X-ray microbeam on the sample in our system, which allows for the measurement of XAFS at various edges from Fe K-edge (7.1 keV) to REE K-edges (38.9 and 43.6 keV for La and Nd, respectively), at the same spot using one optical setup. As a result, HE- $\mu$ -XRF-XAFS analysis enables us to obtain the following: (i) REE patterns (i.e., concentrations of REEs) from La to Dy; (ii) distribution of REEs and other elements with spatial resolutions better than  $1 \mu\text{m}$  without interferences between REEs and other elements; and (iii)  $\mu$ -XAFS at various edges from 7 to 54 keV

including K-edges of REEs and Fe. We applied the method to the REE-enriched SWG sample, which showed that (i) most REEs are adsorbed on clay minerals widely distributed in the grain boundary formed during the weathering of granite and (ii) other REEs are also found in apatite among residual mineral particles during weathering. The REE patterns and La and Nd K-edges EXAFS obtained by HE- $\mu$ -XRF-XAFS at each spot contribute to a better understanding of the geochemical behavior of REEs in the natural system such as the formation of IAD during weathering of granitic rocks.

The proposed method is unique compared with other local analyses for trace elements such as LA-ICP-MS and SIMS in terms of the following: (i) high spatial resolution (better than 1  $\mu$ m); (ii) speciation is possible by XAFS; and (iii) much lower degree of damage by the beam on the sample. Although its application is limited from La to Dy at present, it is expected that further development of the KB mirror and synchrotron radiation X-ray sources at higher energy will enable us to extend the method to entire REEs with sufficient photon flux.

**Author Contributions:** Conceptualization, M.N. and Y.T.; methodology, O.S. and K.N.; validation, T.K.; writing, M.N. and Y.T.; project administration, Y.T.; funding acquisition, Y.T. All authors have read and agreed to the published version of the manuscript.

**Funding:** This research was supported by Grant-in-Aid from the Japan Society for Promotion of Science (JSPS; grant numbers: 22H00166, 22F21313, 22KK0166, and 21J20672). M.N. also acknowledges JSPS Research Fellowships for Young Scientists.

**Data Availability Statement:** Data are contained within the article.

**Acknowledgments:** HE- $\mu$ -XRF-XAFS analysis was conducted by the approval of SPring-8 (proposal Nos.: 2022B0577, 2022B1539, 2022A1507, and 2020A0174).

**Conflicts of Interest:** The authors declare no conflict of interest.

## References

1. McSween, H.Y.; Richardson, S.M.; Uhle, S.M. *Geochemistry: Pathways and Processes*; Columbia University Press: New York, NY, USA, 2003.
2. Henderson, P. *Rare Earth Element Geochemistry*; Elsevier: Amsterdam, The Netherlands, 2013.
3. Takahashi, Y.; Manceau, A.; Geoffroy, N.; Marcus, M.A.; Usui, A. Chemical and structural control of the partitioning of Co, Ce, and Pb in marine ferromanganese oxides. *Geochim. Cosmochim. Acta* **2007**, *71*, 984–1008. [[CrossRef](#)]
4. Goodenough, K.M.; Wall, F.; Merriman, D. The Rare Earth Elements: Demand, Global Resources, and Challenges for Resourcing Future Generations. *Nat. Resour. Res.* **2018**, *27*, 201–216. [[CrossRef](#)]
5. Kashiwabara, T.; Toda, R.; Nakamura, K.; Yasukawa, K.; Fujinaga, K.; Kubo, S.; Nozaki, T.; Takahashi, Y.; Suzuki, K.; Kato, Y. Synchrotron X-ray spectroscopic perspective on the formation mechanism of REY-rich muds in the Pacific Ocean. *Geochim. Cosmochim. Acta* **2018**, *240*, 274–292. [[CrossRef](#)]
6. Borst, A.M.; Smith, M.P.; Finch, A.A.; Estrade, G.; Villanova-de-Benavent, C.; Nason, P.; Marquis, E.; Horsburgh, N.J.; Goodenough, K.M.; Xu, C.; et al. Adsorption of rare earth elements in regolith-hosted clay deposits. *Nat. Commun.* **2020**, *11*, 4386. [[CrossRef](#)]
7. Yamaguchi, A.; Honda, T.; Tanaka, M.; Tanaka, K.; Takahashi, Y. Discovery of ion-adsorption type deposits of rare earth elements (REE) in southwest Japan with speciation of REE by extended X-ray absorption fine structure spectroscopy. *Geochem. J.* **2018**, *52*, 415–425. [[CrossRef](#)]
8. Nagasawa, M.; Qin, H.; Yamaguchi, A.; Takahashi, Y. Local structure of rare earth elements (REE) in marine ferromanganese oxides by extended X-ray absorption fine structure and its comparison with REE in ion-adsorption type deposits. *Chem. Lett.* **2020**, *8*, 909–911. [[CrossRef](#)]
9. Takahashi, Y.; Shimizu, H.; Usui, A.; Kagi, H.; Nomura, M. Direct observation of tetravalent cerium in ferromanganese nodules and crusts by X-ray-absorption near-edge structure (XANES). *Geochim. Cosmochim. Acta* **2000**, *64*, 2929–2935. [[CrossRef](#)]
10. Takahashi, Y.; Kolonin, G.R.; Shironosova, G.P.; Kupriyanova, I.I.; Uruga, T.; Shimizu, H. Determination of the Eu(II)/Eu(III) ratios in minerals by X-ray absorption near-edge structure (XANES) and its application to hydrothermal deposits. *Mineral. Mag.* **2005**, *69*, 179–190. [[CrossRef](#)]
11. Rakovan, J.; Newville, M.; Sutton, S. Evidence of heterovalent europium in zoned Ilallgua apatite using wavelength dispersive XANES. *Am. Mineral.* **2001**, *86*, 697–700. [[CrossRef](#)]
12. Janots, E.; Bernier, F.; Brunet, F.; Muñoz, M.; Trcera, N.; Berger, A.; Lanson, M. Ce(III) and Ce(IV) (re)distribution and fractionation in a laterite profile from Madagascar: Insights from in situ XANES spectroscopy at the Ce L<sub>III</sub>-edge. *Geochim. Cosmochim. Acta* **2015**, *153*, 134–148. [[CrossRef](#)]

13. Konagaya, R.; Kawamura, N.; Yamaguchi, A.; Takahashi, Y. Highly-sensitive Analysis of Fluorescence XANES at Europium (Eu) L<sub>III</sub> -edge for the Determination of Oxidation State for Trace Amount of Eu in Natural Samples by Bragg-type Crystal Analyzer System. *Chem. Lett.* **2021**, *50*, 1570–1572. [[CrossRef](#)]
14. Takahashi, Y.; Yamamoto, M.; Yamamoto, Y.; Tanaka, K. EXAFS study on the cause of enrichment of heavy REEs on bacterial cell surfaces. *Geochim. Cosmochim. Acta* **2010**, *74*, 5443–5462. [[CrossRef](#)]
15. Manceau, A.; Lanson, M.; Takahashi, Y. Mineralogy and crystal chemistry of Mn, Fe, Co, Ni, and Cu in a deep-sea Pacific polymetallic nodule. *Am. Mineral.* **2014**, *99*, 2068–2083. [[CrossRef](#)]
16. Marcus, M.A.; Toner, B.M.; Takahashi, Y. Forms and distribution of Ce in a ferromanganese nodule. *Mar. Chem.* **2018**, *202*, 58–66. [[CrossRef](#)]
17. Kirkpatrick, P.; Baez, A.V. Formation of optical images by X-rays. *J. Opt. Soc. Am.* **1948**, *38*, 766–774. [[CrossRef](#)]
18. Nitta, K.; Sekizawa, O. BL37XU (Trace Element Analysis). In *Spring-8/SACLA Annual Report FY2018*; RIKEN/JASRI: Hyogo, Japan, 2019; Volume 18, pp. 64–66.
19. Rosa, A.D.; Kuppenko, I.; Hernandez, J.A.; Forestier, A.; Muñoz, M.; Morard, G.; Bouhifd, M.A.; Lomachenko, K.A.; Torchio, R.; Chumakov, A.; et al. New Opportunities for Earth Science at the Extremely Brilliant Source of the European Synchrotron Radiation Facility. *Synchrotron Radiat. News* **2022**, *35*, 8–16. [[CrossRef](#)]
20. De Pauw, E.; Tkalec, B.J.; Tack, P.; Vekemans, B.; Di Michiel, M.; Brenker, F.E.; Vincze, L. High energy synchrotron X-ray fluorescence trace element study of a millimeter-sized asteroidal particle in preparation for the Hayabusa2 return sample analyses. *Spectrochim. Acta Part B At. Spectrosc.* **2022**, *188*, 106346. [[CrossRef](#)]
21. Quartieri, S.; Dalconi, M.C.; Boscherini, F.; Oberti, R.; D’Acapito, F. Changes in the local coordination of trace rare-earth elements in garnets by high-energy XAFS: New data on dysprosium. *Phys. Chem. Miner.* **2004**, *31*, 162–167. [[CrossRef](#)]
22. Pearce, N.J.G.; Perkins, W.T.; Westgate, J.A.; Gorton, M.P.; Jackson, S.E.; Neal, C.R.; Chenery, S.P. A Compilation of New and Published Major and Trace Element Data for NIST SRM 610 and NIST SRM 612 Glass Reference Materials. *Geostand. Geoanal. Res.* **1997**, *21*, 115–144. [[CrossRef](#)]
23. Badanina, E.V.; Trumbull, R.B.; Dulski, P.; Wiedenbeck, M.; Veksler, I.V.; Syritso, L.F. The behavior of rare-earth and lithophile trace elements in rare-metal granites: A study of fluorite, melt inclusions and host rocks from the Khangilay complex, Transbaikalia, Russia. *Can. Mineral.* **2006**, *44*, 667–692. [[CrossRef](#)]
24. Tanaka, K.; Takahashi, Y.; Shimizu, H. Determination of rare earth element in carbonate using laser-ablation inductively-coupled plasma mass spectrometry: An examination of the influence of the matrix on laser-ablation inductively-coupled plasma mass spectrometry analysis. *Anal. Chim. Acta* **2007**, *583*, 303–309. [[CrossRef](#)] [[PubMed](#)]
25. Zhu, Y.; Mongelli, G.; Sinisi, R.; Yim, Y.H. Editorial: Analytical chemistry of rare earth elements (REEs). *Front. Chem.* **2020**, *10*, 1631. [[CrossRef](#)]
26. Wallrich, B.M.; Miller, C.F.; Gualda, G.A.R.; Miller, J.S.; Hinz, N.H.; Faulds, J.E. Volcano-pluton connection: Perspectives on material and process linkages, Searchlight pluton and Highland Range volcanic sequence, Nevada, USA. *Earth-Sci. Rev.* **2023**, *238*, 104361. [[CrossRef](#)]
27. Terashima, S.; Usui, A.; Imai, N. 2 new GSJ geochemical reference samples—Syenite JSY-1 and manganese-nodule JMN-1. *Geostand. Newsl.* **1995**, *19*, 221–229. [[CrossRef](#)]
28. Verlaan, P.A.; Cronan, D.S. Origin and variability of resource-grade marine ferromanganese nodules and crusts in the Pacific Ocean: A review of biogeochemical and physical controls. *Geochemistry* **2022**, *82*, 125741. [[CrossRef](#)]
29. Nagasawa, M.; Takahashi, Y. Vertical migration and enrichment of rare earth elements (REEs) in ion-adsorption type mineralization in Japan based on REE speciation analysis. 2023, *in press*.
30. Takahashi, Y.; Yoshida, H.; Sato, N.; Hama, K.; Yusa, Y.; Shimizu, H. W- and M-type tetrad effects in REE patterns for water-rock systems in the Tono uranium deposit, central Japan. *Chem. Geol.* **2002**, *184*, 311–335. [[CrossRef](#)]
31. The Center for X-Ray Optics (CXRO). X-Ray Interactions with Matter. Available online: [https://henke.lbl.gov/optical\\_constants/](https://henke.lbl.gov/optical_constants/) (accessed on 19 May 2023).
32. Solé, V.A.; Papillon, E.; Cotte, M.; Walter, P.; Susini, J. A multiplatform code for the analysis of energy-dispersive X-ray fluorescence spectra. *Spectrochim. Acta Part B At. Spectrosc.* **2007**, *62*, 63–68. [[CrossRef](#)]
33. Anders, E.; Grevesse, N. Abundances of the elements—Meteoritic and solar. *Geochim. Cosmochim. Acta* **1989**, *53*, 197–214. [[CrossRef](#)]
34. Nakada, R.; Tanimizu, M.; Takahashi, Y. Difference in the stable isotopic fractionations of Ce, Nd, and Sm during adsorption on iron and manganese oxides and its interpretation based on their local structures. *Geochim. Cosmochim. Acta* **2013**, *121*, 105–119. [[CrossRef](#)]
35. Zabinsky, S.I.; Rehr, J.J.; Ankudinov, A.; Albers, R.C.; Eller, M.J. Multiple-scattering calculations of X-ray-absorption spectra. *Phys. Rev. B* **1995**, *52*, 2995–3009. [[CrossRef](#)]
36. O’Day, P.A.; Rehr, J.J.; Zabinsky, S.I.; Brown, G.E. Extended X-ray absorption fine structure (EXAFS) analysis of disorder and multiple scattering in complex crystalline solids. *J. Am. Chem. Soc.* **1994**, *116*, 2938–2949. [[CrossRef](#)]
37. Li, W.; Yamada, S.; Hashimoto, T.; Okumura, T.; Hayakawa, R.; Nitta, K.; Sekizawa, O.; Suga, H.; Uruga, T.; Ichinohe, Y.; et al. High-sensitive XANES analysis at Ce L<sub>2</sub>-edge for Ce in high-Ti geological samples using transition-edge sensors. *Anal. Chim. Acta* **2023**, *1240*, 340755. [[CrossRef](#)]

38. Abe, Y.; Iizawa, Y.; Terada, Y.; Adachi, K.; Igarashi, Y.; Nakai, I. Detection of uranium and chemical state analysis of individual radioactive microparticles emitted from the Fukushima nuclear accident using multiple synchrotron radiation X-ray analyses. *Anal. Chem.* **2014**, *86*, 8521–8525. [[CrossRef](#)] [[PubMed](#)]
39. Matsushita, T.; Hashizume, H. X-Ray Monochromators. *Handb. Synchrotron Radiat.* **1983**, *1*, 261–314.
40. Boone, M.N.; Van Assche, F.; Vanheule, S.; Cipiccia, S. Full-field spectroscopic measurement of the X-ray beam from a multilayer monochromator using a hyperspectral X-ray camera research papers. *J. Synchrotron Rad.* **2020**, *27*, 110–118. [[CrossRef](#)] [[PubMed](#)]
41. Firester, A.H.; Heller, M.E.; Sheng, P. Knife-edge scanning measurements of subwavelength focused light beams. *Appl. Opt.* **1977**, *16*, 1971. [[CrossRef](#)]
42. Takeuchi, A.; Suzuki, Y.; Uesugi, K. Differential-phase-contrast knife-edge scan method for precise evaluation of X-ray nanobeam. *Jpn. J. Appl. Phys.* **2015**, *54*, 092401. [[CrossRef](#)]
43. Takahashi, Y.; Shimizu, H.; Kagi, H.; Yoshida, H.; Usui, A.; Nomura, M. A new method for the determination of Ce<sup>III</sup>/Ce<sup>IV</sup> ratios in geological materials; application for weathering, sedimentary and diagenetic processes. *Earth Planet. Sci. Lett.* **2000**, *182*, 201–207. [[CrossRef](#)]
44. Sanematsu, K.; Watanabe, Y. Characteristics and genesis of ion adsorption-type rare earth element deposits. *Rev. Econ. Geol.* **2016**, *18*, 55–79.
45. Liu, X.; Tournassat, C.; Grangeon, S.; Kalinichev, A.G.; Takahashi, Y.; Marques Fernandes, M. Molecular-level understanding of metal ion retention in clay-rich materials. *Nat. Rev. Earth Environ.* **2022**, *3*, 461–476. [[CrossRef](#)]
46. Frietsch, R.; Perdahl, J.A. Rare earth elements in apatite and magnetite in Kiruna-type iron ores and some other iron ore types. *Ore Geol. Rev.* **1995**, *9*, 489–510. [[CrossRef](#)]
47. Nishihata, Y.; Kamishima, O.; Kubozono, Y.; Maeda, H.; Emura, S. XAFS in the high-energy region. *J. Synchrotron Radiat.* **1998**, *5*, 1007–1009. [[CrossRef](#)]
48. Ohta, A.; Kagi, H.; Nomura, M.; Shitsuno, H.; Kawabe, I. Coordination study of rare earth elements on Fe oxyhydroxide and Mn dioxides: Part ii. Correspondence of structural change to irregular variations of partitioning coefficients and tetrad effect variations appearing in interatomic distances. *Am. Mineral.* **2009**, *94*, 476–486. [[CrossRef](#)]
49. Kumar, Y.; Tripathi, S.; Nand, M.; Jangir, R.; Srihari, V.; Das, A.; Singh, R.; Deshpande, U.; Jha, S.N.; Arya, A. Structural and optical properties of Nd doped LaPO<sub>4</sub>. *J. Alloys Compd.* **2022**, *925*, 166772. [[CrossRef](#)]
50. Cole, J.M.; Newport, R.J.; Bowron, D.T.; Pettifer, R.F.; Mountjoy, G.; Brenna, T.; Saunders, G.A. A rare-earth K-edge XAFS study of rare-earth phosphates glasses, (R<sub>2</sub>O<sub>3</sub>)<sub>x</sub>(P<sub>2</sub>O<sub>5</sub>)<sub>1-x</sub>, x = 0.187–0.239, R = La, Nd, Sm, Eu, Gd, Dy, Er. *J. Phys. Condens. Matter* **2001**, *13*, 6659–6674. [[CrossRef](#)]
51. Sanematsu, K.; Kon, Y.; Imai, A. Influence of phosphate on mobility and adsorption of REEs during weathering of granites in Thailand. *J. Asian Earth Sci.* **2015**, *111*, 14–30. [[CrossRef](#)]
52. Mukai, H.; Kon, Y.; Sanematsu, K.; Takahashi, Y.; Ito, M. Microscopic analyses of weathered granite in ion-adsorption rare earth deposit of Jianxi Province, China. *Sci. Rep.* **2020**, *10*, 20194. [[CrossRef](#)] [[PubMed](#)]
53. Kowall, T.; Foglia, F.; Helm, L.; Merbach, A.E. Molecular dynamics simulation study of lanthanide ions Ln<sup>3+</sup> in aqueous solution including water polarization. Change in coordination number from 9 to 8 along the series. *J. Am. Chem. Soc.* **1995**, *117*, 3790–3799. [[CrossRef](#)]
54. Kanazawa, Y.; Kamitani, M. Rare earth minerals and resources in the world. *J. Alloys Compd.* **2006**, *408*, 1339–1343. [[CrossRef](#)]
55. Habenschuss, A.; Spedding, F.H. The coordination (hydration) of rare earth ions in aqueous chloride solutions from X-ray diffraction. III. SmCl<sub>3</sub>, EuCl<sub>3</sub>, and series behavior. *J. Chem. Phys.* **1980**, *73*, 442–450. [[CrossRef](#)]

**Disclaimer/Publisher’s Note:** The statements, opinions and data contained in all publications are solely those of the individual author(s) and contributor(s) and not of MDPI and/or the editor(s). MDPI and/or the editor(s) disclaim responsibility for any injury to people or property resulting from any ideas, methods, instructions or products referred to in the content.